Lawrence Berkeley National Laboratory
LBL Publications

Title

Core-Level Spectroscopy with Hard and Soft X–rays on Phosphorus-Containing Compounds for Energy Conversion and Storage

Authors

Wibowo, Romualdus Enggar

Garcia-Diez, Raul

van der Merwe, Marianne

et al.

Peer reviewed

Core-Level Spectroscopy with Hard and Soft X-rays on Phosphorus-Containing Compounds for Energy Conversion and Storage

Romualdus Enggar Wibowo,* Raul Garcia-Diez, Marianne van der Merwe, Daniel Duarte-Ruiz, Yang Ha, Roberto Félix, Anna Efimenko, Tomas Bystron, Martin Prokop, Regan G. Wilks, Karel Bouzek, Wanli Yang, Caterina Cocchi,* and Marcus Bär*

ACCESS | Metrics & More | Article Recommendations | Supporting Information

ABSTRACT: The electronic properties of nine solid phosphorus (P)-containing compounds with varying oxidation states and chemical environments, including $GaP^{(-III)}$, $InP^{(-III)}$, red-$P^{(0)}$, $H_3P^{(III)}O_3$, $Na_2H_2P_2^{(IV)}O_6$, $H_3P^{(V)}O_4$, $KH_2P^{(V)}O_4$, $Na_2HP^{(V)}O_4$, and $InP^{(V)}O_4$, are investigated using X-ray absorption near-edge structure (XANES) spectroscopy in the hard (P K-edge) and soft X-ray regime (P $L_{2,3}$-edge). We find shifts in the absorption-edge positions and correlate them with the ligands surrounding the P atom, likely causing a different core−hole interaction screening for different compounds. Complementing the experimental analysis, *ab initio* many-body calculations of XANES spectra provide insights into the excitonic nature of the observed spectral features and their impact on the electronic structure of the materials. Furthermore, we report on P K-edge XANES

measurements on aqueous phosphorus-containing acids, including H_3PO_3, H_3PO_4, and their mixtures. At first sight, the spectra of the aqueous acids are similar to those of their solid counterparts. However, close inspection reveals a slight red shift of the absorption edge and the presence of fewer spectral features compared with spectra of the respective solids. Mixtures of aqueous acids display spectral features corresponding to the individual components, indicating the potential for speciation and quantification through fingerprinting.
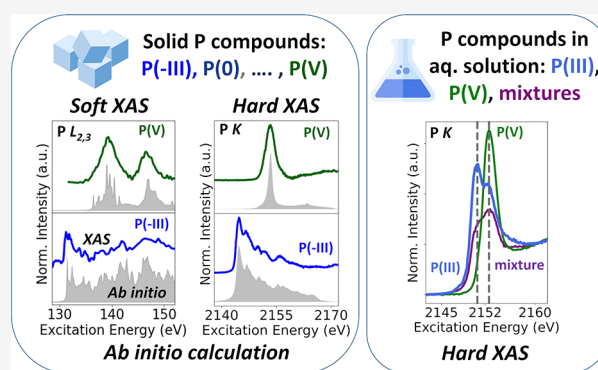
1. INTRODUCTION

Phosphorus (P)-containing compounds exist in a wide range of forms and are indispensable for many aspects of life. Phosphates (i.e., salts containing phosphate ions, PO_4^{3-}) are part of the human's deoxyribonucleic acid (DNA) and are responsible for energy storage via ATP (adenosine triphosphate, $C_{10}H_{16}N_5O_{13}P_3$). Phosphates are also used in fertilizers (e.g., $Ca_3(PO_4)_2$, $FePO_4$). In automotive industries, zinc dialkyldithiophosphate (ZDDP, $C_{16}H_{36}O_4P_2S_4Zn$) is often utilized as an additive for lubricating oil as an antiwear and antioxidant.[1−3] Multiple electrochemical energy storage technologies also use P-containing materials. For instance, metal phosphide-based materials (e.g., CuP, FeP, CoP), or black phosphorus carbon composites (e.g., black-phosphorus/graphite/carbon-nantotubes), are currently being developed as anode materials for Li-ion and Na-ion batteries.[4−6] For fuel cell technologies, phosphorus-based acids such as H_3PO_4 have been used as a medium ensuring electron transfer and are employed in phosphoric acid fuel cells (PAFC)[7] and high-temperature polymer electrolyte membrane fuel cells (HT-PEMFCs).[8] Solid CsH_2PO_4 is exploited in solid-acid fuel cells (SAFC).[9] Another work has attempted to explore the possibilities of using other phosphorus-containing acids

(e.g., H_3PO_3) as electrolytes for fuel cells operating at elevated temperatures.[10] For the generation of hydrogen via photocatalytic water splitting applications, P-containing compounds, such as black phosphorus and red phosphorus, are being extensively developed as photocatalyst materials.[11,12] Additionally, phosphides (such as InP and GaP) are oftentimes used as photocathodes[13] while several phosphates (e.g., cobalt phosphates, iron phosphates) are used as cocatalysts for photocatalytic water splitting.[13] Furthermore, P-based materials, such as GaInP and black phosphorus, are also utilized as photovoltaic materials.[14,15]

For many such applications, X-ray absorption near-edge structure (XANES) spectroscopy has been frequently used to identify phosphorus compounds in a given sample or to investigate changes in the properties of compounds during or after certain treatments. For instance, P K-edge XANES has
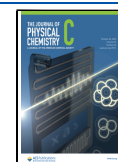
been extensively adopted for the speciation of phosphorus compounds in soil and other minerals.[16−22] It was also used in studies of P-based anode materials in Na-ion and Li-ion batteries[5,6] and in *operando* investigations of organic/inorganic hybrid insertion-type material for Li-ion batteries.[23] Similarly, several P $L_{2,3}$-edge XANES investigations (also called near-edge X-ray absorption fine structure, or NEXAFS, for P $L_{2,3}$-edge studies using soft X-rays) have been performed for the speciation of P-containing compounds, such as in soils or in antiwear applications.[1−3,24]

Despite the increased use of spectroscopic reference data from the P K-edge and $L_{2,3}$-edge in recent years, the vast majority of the reported investigations are focused on solid P(V)-based compounds, mainly related to the study of orthophosphates in soil and minerals,[16−18,25] in antiwear films,[1−3,26] or in phosphate-containing glasses.[24,27] This translates into a limited number of XANES studies for P-containing compounds having a wider range of nominal P oxidation states. Exceptions included some works on phosphide semiconductors (P oxidation state of (-III)),[28,−31] elemental phosphorus (P oxidation state of (0)),[32] or standardization of minerals containing P-compounds using X-ray absorption spectroscopy.[25] Investigations of phosphorus-containing compounds in the liquid state are just as scarce, except for a few P K-edge XANES investigations and extended X-ray absorption fine structure studies on phosphate ions in solution.[33,−35] Yet, P-containing liquids (e.g., H_3PO_4) are being used for state-of-the-art energy conversion (in PAFCs and HT-PEMFCs), and so as part of an effort to further advance the knowledge of such systems, we present a systematic XANES study of the P K-edge and P $L_{2,3}$-edge of P-containing compounds characterized by a wide range of oxidation states and ligand groups, in both solid and liquid states.

The P K-edge and P $L_{2,3}$-edge XANES measurements were performed on nine solid compounds with different chemical environments and oxidation states ranging from P in an oxidation state of (-III) to P in an oxidation state of (V), namely, $GaP^{(-III)}$, $InP^{(-III)}$, red-$P^{(0)}$, $H_3P^{(III)}O_3$, $Na_2H_2P_2^{(IV)}O_6$, $H_3P^{(V)}O_4$, $KH_2P^{(V)}O_4$, $Na_2HP^{(V)}O_4$, and $InP^{(V)}O_4$. In particular, $H_3P^{(III)}O_3$ and $Na_2H_2P^{(IV)}_2O_6$ were investigated, since studies on these materials (or other materials with P in a nominal oxidation state of P(III) and P(IV)) are very scarce. Additionally, $H_3P^{(III)}O_3$ and $H_3P^{(V)}O_4$ are important for HT-PEMFC research, with several studies indicating the possible conversion of $H_3P^{(V)}O_4$ electrolyte to phosphorus compounds having a lower oxidation state (e.g., $H_3P^{(III)}O_3$) during the operation, which may subsequently poison the Pt catalyst.[36−38] The adsorption of $H_3P^{(III)}O_3$ on a Pt surface at ambient temperature has already been proven electrochemically[39] and indicated spectroscopically through the combination of X-ray absorption spectroscopy at P L_3-edge and density functional theory.[40] Hence, P K-edge XANES measurements on these compounds will be beneficial (and a prerequisite) for future *operando* studies of these systems. Furthermore, P K-edge XANES was also performed on aqueous phosphoric acid (H_3PO_4), aqueous phosphorus acid (H_3PO_3), and their mixtures. These measurements were carried out to observe any potential (chemical and electronic) structure change occurring to P-containing acids in solution as compared to their solid states as well as to determine the possibility of speciation within aqueous mixtures, again as a foundation for future *operando* studies. The experimental analysis is complemented by state-of-the-art *ab initio* calculations of P K- and $L_{2,3}$-edge XANES spectra of four solid-state reference compounds, namely, red-P, InP, GaP, and $InPO_4$. The purpose of these calculations is to shed light on the (excitonic) nature of the absorption maxima and to connect the spectral fingerprints of the materials to their electronic structure for future reference. As such, this work provides insight into the speciation of P-containing compounds, which can be beneficial for future studies on P-containing materials.

2. MATERIALS AND METHODS

2.1. Materials. Nine solid P-containing compounds with different chemical environments and oxidation states were prepared: gallium phosphide (GaP), indium phosphide (InP), red phosphorus (P, red phosphorus, ≥97.0%, Merck, hereafter referred to as "red-P"), phosphorus acid (crystalline H_3PO_3, 99%, Merck), disodium hypophosphate ($Na_2H_2P_2O_6\cdot10H_2O$, hereafter referred to as "$Na_2H_2P_2O_6$"), phosphoric acid (crystalline H_3PO_4, 99.99%, Merck), potassium hydrogen phosphate (KH_2PO_4, ≥99.0%, Mallinckrodt), sodium dihydrogen phosphate ($Na_2HPO_4\cdot12H_2O$, J.T Baker, hereafter referred to as "Na_2HPO_4"), and indium phosphate ($InPO_4$, 98%, Alfa Aesar). GaP and InP were synthesized with the method previously used in ref 41. $Na_2H_2P_2O_6$ was synthesized according to the method previously used by Prokop et al.[38] Other details on these solid compounds (e.g., CAS number of the compounds and expected electronic configuration) are given in Table S1 in the Supporting Information (SI). Prior to the XANES measurement, to increase the sample surface area, all powder samples were ground into fine powder using a mortar and pestle. The grinding process was carried out in an inert atmosphere (inside an argon-purged glovebox) to prevent oxidation during grinding.

The aqueous compounds with concentrations of 1 mol dm^{-3} were prepared by diluting either crystalline H_3PO_3 (99 wt %, Merck) or crystalline H_3PO_4 (99.99 wt %, Merck) in Milli-Q water (Q-POD, conductivity ∼0.055 $\mu S\ cm^{-1}$) until the concentration of interest was achieved. Additionally, aqueous mixtures of H_3PO_3 and H_3PO_4, (i) 1 mol of $dm^{-3}\ H_3PO_3$ + 1 mol of $dm^{-3}\ H_3PO_4$ and (ii) 0.1 mol of $dm^{-3}\ H_3PO_3$ + 1 mol of $dm^{-3}\ H_3PO_4$, were prepared. Prior to the measurement, the aqueous samples were deaerated by purging the solution with N_2 (purity ≥99.996%) for 30 min to avoid the possible oxidation by O_2 in the solution.

2.2. P K-Edge XANES on Solid P-Containing Compounds. The P K-edge XANES measurements of the solid P-containing compounds were conducted in reflection geometry using the SpAnTeX end-station[42] (for H_3PO_3, $Na_2H_2P_2O_6$, H_3PO_4, KH_2PO_4, and $InPO_4$) or the HiKE end-station[43] (for GaP, InP, and red-P). Both setups are located at the KMC-1 beamline[44] of BESSY II, operated by HZB. The incoming X-rays were monochromatized by using a Si(111) double-crystal monochromator. The spectra were recorded in partial fluorescence yield (PFY) mode by setting the Bruker XFlash 4010 fluorescence SDD to detect P K_α fluorescence, i.e., photon with the energy between 1.9 and 2.1 keV, with an energy resolution of 135 eV. Note that the detector resolution does not determine the recorded P K-edge XANES energy resolution, as this is mainly governed by the excitation energy resolution, natural line width of the transition, and the experimental energy steps. For this experiment, the resolution was ∼0.58 eV (see details and consideration for the energy resolution in Section S9 of the SI). Simultaneously with the

PFY-XANES, spectra were also obtained in total electron yield (TEY) mode by recording the sample compensation current using an electrometer (Keithley, 6517B). For each spectrum, a linear background was fitted and subtracted, before normalization. The recorded excitation energy was calibrated by conducting hard X-ray photoelectron spectroscopy (HAXPES) measurements on a Au foil using 2120 and 2230 eV excitations (i.e., the start and end energies of the P K-edge XANES scan) and setting the binding energy of the Au $4f_{7/2}$ core level to 84.00 eV.[45] To validate the quality of the recorded data, the spectra obtained in this study are compared with those previously published in the literature.[27,28,30,32,46] The comparison is presented in Section S7 of the SI, highlighting a strong agreement between the P K-edge spectra obtained in our study and the reference spectra (as shown in Figure S8).

Additionally, to facilitate the comparison between experimental data and *ab initio* calculation results, arctan backgrounds representing the electronic transitions to continuum states, which are not modeled, were fitted to the measured spectra and subtracted. The center of the arctan was constrained at the absorption edge of the spectrum. A linear function is added to the arctan background to account for the experimental background signal. This procedure was performed by using a Python script based on the LMFIT package.[47]

The absorption-edge positions are derived using the inflection point of the XANES onset (determined by the maxima of the first derivative as presented in Figure S1 in the SI), as typically conducted when evaluating hard XANES data.[34,48,49] Detailed insights into the considerations for the absorption-edge position determination, along with a comparison of absorption-edge positions derived by using the intersection of a linear extrapolation of the rising edge caused by the first absorption maxima and the spectral background (as presented in Figure S2 in the SI and as often used in the soft X-ray community), are provided in Section S9 of the SI.
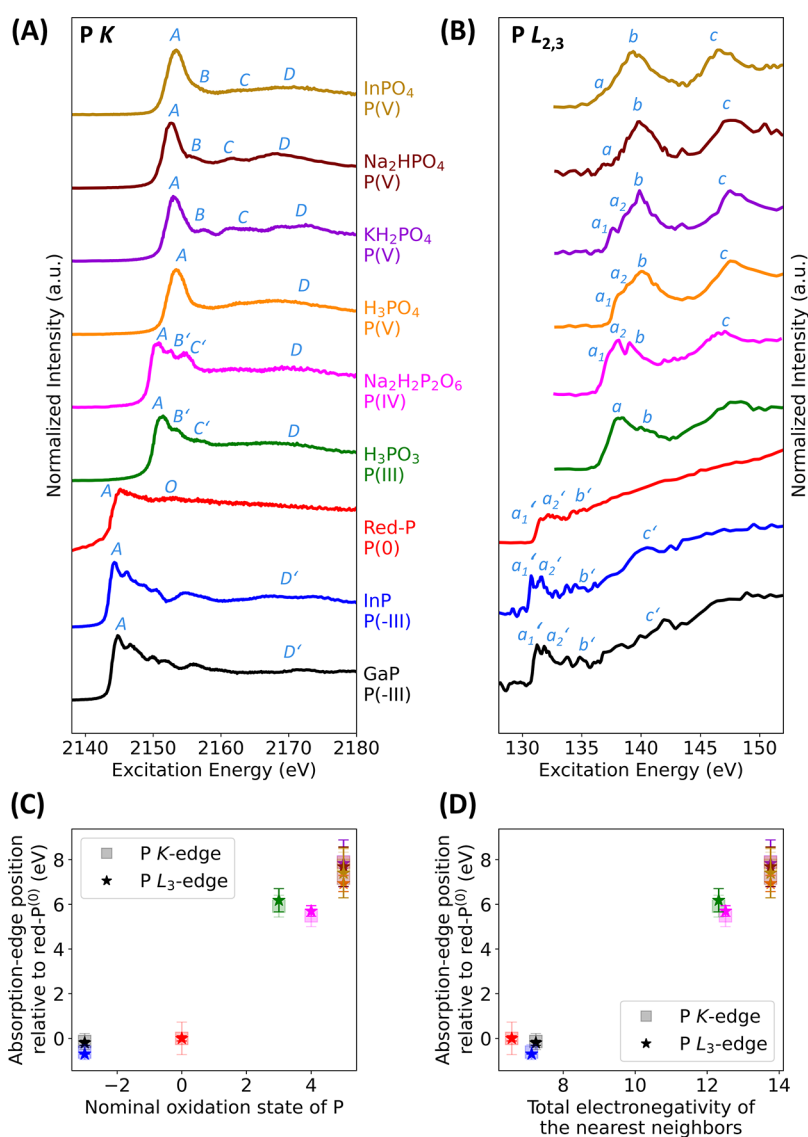
2.3. P $L_{2,3}$-Edge XANES on Solid P-Containing Compounds. P $L_{2,3}$-edge measurements of the solid P-containing compounds were performed in the iRIXS endstation,[50] at beamline 8.0.1 of the Advanced Light Source (ALS),[51] Lawrence Berkeley National Laboratory. The measurements were performed using the low-energy grating of the spherical grating monochromator of this undulator beamline. For detection, a channeltron or a high-throughput iRIXS spectrometer equipped with a CCD (charge-coupled device) camera was employed (see details in ref 50). The data collected from the spectrometer is recorded as a resonant inelastic X-ray scattering (RIXS) map, for a subsequent determination of PFY-XANES. Hence, the XANES spectra were obtained in both total fluorescence yield (TFY, i.e., the data recorded by using a channeltron) and PFY mode. While in TFY mode all X-ray/UV photons emitted from the sample will be collected to derive the XANES spectrum, in PFY mode the energy-dispersive spectrometer allows to only select P $L_{2,3}$-fluorescence photons. Details on PFY signal integration from RIXS maps are given in the SI in Figure S3. For data evaluation, PFY-XANES was used instead of TFY-XANES to avoid contributions from elastically scattered photons that tend to be significant in this energy region (see Figure S3), thus affecting (in the worst case: dominating) the XANES data. A comparison of the PFY- and TFY-XANES data is shown in Figure S4, illustrating that PFY-derived spectra possess a higher signal-to-noise ratio compared to that of the TFY

spectra. In addition, simultaneous with the PFY and TFY measurements, spectra were also obtained in TEY mode by recording the sample compensation current.

The XANES excitation energy was calibrated by aligning the absorption spectrum of InP to the corresponding spectrum reported in ref 31. Similar to P K-edge XANES, a linear background is fitted and subtracted before the spectra are normalized. Additionally, for an accurate comparison between experimental data and *ab initio* calculated spectra, double arctan backgrounds,[52,53] representing the P 2p doublet electronic transition to continuum states, are fitted and subtracted. For compounds that show strong features corresponding to P 3s → P $2p_{3/2}$- and P 3s → P $2p_{1/2}$-derived transitions, the center of each of the double arctan backgrounds is constrained to the energy corresponding to the spectral feature of these transitions. For compounds that do not show a strong doublet feature (i.e., only a convolution of these spectral features can be observed), the center of the second arctan background is kept constant at the absorption-edge position of the respective compounds. The center of the first arctan background is estimated through the subtraction of the compound respective absorption-edge position to the P 2p doublet separation of the compounds, which was approximated from the National Institute of Standards and Technology (NIST) database.[54,−56] Absorption-edge positions are determined using the same procedure as for the P K-edge, as detailed in section 2.2. Further details and considerations for absorption-edge position determination can be found in Figures S5 and S6 and Section S9 of the SI. Moreover, for a better representation of the observed spectral background, the arctan is modified by adding a linear component. A Python script based on the LMFIT package was used to perform the aforementioned procedure.

To validate the quality of the recorded data, the spectra obtained in this study are compared with those previously published in the literature.[25,29,32,57] The comparison is presented in Section S7 of the SI, highlighting a strong agreement between the P K-edge spectra obtained in our study and the reference spectra (as shown in Figure S9).

2.4. P K-Edge XANES of Aqueous H_3PO_4 and H_3PO_3 Acid−Based Solutions. P K-edge XANES measurements of aqueous H_3PO_4 and H_3PO_3 acid−based solutions were carried out using custom-designed *in situ* cells made of PEEK that allow the study of liquids, either at the HiKE end-station at the KMC-1 bending magnet beamline (for the 1 mol dm$^{−3}$ H_3PO_3 and both of the H_3PO_3 + H_3PO_4 solution mixtures detailed in Section 2.1) or at the OÆSE end-station located at the two-color EMIL beamline (for the 1 mol dm$^{−3}$ H_3PO_4 solution) at the BESSY II synchrotron radiation facility operated by HZB. Details on the liquid *in situ* cells that utilize a 12 μm-thick Kapton membrane (Sigma-Aldrich), as an X-ray transparent window separating the P-containing solutions at atmospheric pressure from the vacuum conditions of the beamline and diagnostic, can be found in Section S6 and Figure S7 of the SI. For the measurements at the HiKE end-station, a similar experimental setup as detailed in Section 2.2 was used. For the XANES measurement in the OÆSE end-station, the hard X-ray branch of the EMIL beamline, i.e., the CPMU17 undulator in combination with a Si(111) double-crystal monochromator and a set of optical mirrors, provides photons of the required energy to the sample. Spectra were recorded in TFY mode using a photodiode (ODD-AXU-010, Opto Diode). For energy calibration, the P K-edge XANES spectrum of solid

Figure 1. (A) P K-edge and (B) P $L_{2,3}$-edge PFY-XANES of solid P-containing compounds. Labels of spectral features shown in (A) and (B) are discussed in the text. Note that different excitation energy scales are used for (A) and (B). Absorption-edge positions derived from the P K- and P $L_{2,3}$-edge spectra shown in (A) and (B) are depicted as a function of the (C) nominal oxidation state of P and of (D) total electronegativity of the nearest P neighbors. The same color codes used in (A) and (B) are used for (C) and (D). The experimental uncertainty for the absorption-edge positions varies between ±0.67 and ±0.93 eV for the P K-edge and between ±0.14 and ±1.12 eV for the P L_3-edge values. Details for the determination of the uncertainty can be found in Section S9 of the SI. Note that for (C) and (D), the absorption-edge positions of H_3PO_4, KH_2PO_4, Na_2HPO_4, and $InPO_4$ are closely overlapping with each other (the derived absorption-edge positions are listed in Tables S3 and S4 in the SI).

InP was recorded and aligned to the calibrated InP spectrum, from the measurement described in Section 2.2.

To validate the quality of the recorded data, the spectra obtained in this study are compared with those previously published in the literature.[35] The comparison is presented in Section S7 of the SI, highlighting a strong agreement between the P K-edge spectra obtained in our study and the reference spectra (as shown in Figure S10).

2.5. *Ab Initio* Calculations of P K- and $L_{2,3}$-Edge XANES. The calculations of XANES spectra presented in this work are performed in the framework of many-body perturbation theory with the solution of the Bethe−Salpeter equation (BSE) on top of the electronic structure computed from all-electron density functional theory (DFT). The BSE is the equation of motion for the two-particle correlation

function. In practice, the problem is cast into an effective two-particle time-independent Schrödinger equation ruled by the effective BSE Hamiltonian $\hat{H}^{BSE} = \hat{H}^{diag} + \hat{H}^{dir} + \hat{H}^x$, where the first term ($\hat{H}^{diag}$) accounts for single-particle transitions and the other two include the electron−hole Coulomb attraction ($\hat{H}^{dir}$) and exchange repulsion ($\hat{H}^x$).[58,59] The BSE is considered the state-of-the-art method for *ab initio* optical and core-level spectroscopy in condensed matter. The explicit inclusion of core electrons in the underlying DFT step enables the direct calculation of the core-level-to-conduction band transitions matrix elements from first principles.[50] These transition coefficients enter the expression of the imaginary part of the macroscopic dielectric function, providing information about the absorption of the system. The spectra calculated from the BSE are aligned with the experimental

spectra considering the first absorption maximum as a reference. For a comparison, XANES spectra are also calculated using the independent-particle approach (IPA), in which the effects from excitonic states are neglected. In this approach, two Coulombs terms in the BSE Hamiltonian are neglected and only the diagonal term in the BSE Hamiltonian is considered ($\hat{H}^{BSE} = \hat{H}^{diag}$).

DFT and BSE calculations are performed with the all-electron full-potential code **exciting**[60] taking input structures from the Materials Project database,[61] entries mp-157 for red-P, mp-2490 for GaP, mp-20351 for InP, and mp-7566 for InPO$_4$. We employ the Perdew–Burke–Ernzerhof (PBE) functional[62] to approximate the exchange–correlation potential. The Brillouin zone is sampled using a homogeneous k-grid of $6 \times 6 \times 6$ for InP and red-P, and $4 \times 4 \times 4$ for GaP and InPO$_4$. The adopted muffin tin radii for the atoms are 2.5 bohr for In and 2.1 bohr for P in InP, 2.2 bohr for Ga and 2.0 bohr for P in GaP, 2.6 bohr for In, 1.4 bohr for O, and 1.5 bohr for P in InPO$_4$, and 2.0 Bohr for P in red phosphorus. To ensure converged results, a plane-wave cutoff such that $R^{min}_{MT} \times G_{MAX}$ = 8 (7) for InP and red-P (GaP and InPO$_4$) is taken. For the BSE calculations, we use a Γ-shifted k-mesh with $6 \times 6 \times 6$ points for InP and GaP, $4 \times 4 \times 4$ for InPO$_4$, and $5 \times 5 \times 5$ for red-P. The screened Coulomb potential is computed from the random-phase approximation including 50 empty bands. We include transitions from core levels to conduction bands within an energy range of 25 eV above the conduction band minimum. The calculated projected densities of states of these P-containing compounds can be found in Figure S11 in the SI.

3. RESULTS AND DISCUSSION

3.1. Solid P-Containing Compounds: GaP$^{(-III)}$, InP$^{(-III)}$, Red-P$^{(0)}$, H$_3$P$^{(III)}$O$_3$, Na$_2$H$_2$P$_2^{(IV)}$O$_6$, H$_3$P$^{(V)}$O$_4$, KH$_2$P$^{(V)}$O$_4$, Na$_2$HP$^{(V)}$O$_4$, and InP$^{(V)}$O$_4$. The P K-edge XANES spectra (Figure 1A) correspond to the electronic transition from P 1s electrons into unoccupied states formed by P 3s-derived states and other electronic states from ligands. All P K-edge XANES spectra display a distinct narrow white line (feature A) and a broader feature at around 2169 eV (D and D′, except for red-P). Some compounds show other weaker features following the white line (e.g., B, C). Feature A corresponds to the t_2^* transition, which is the transition from P 1s electrons into unoccupied sp^3-hybridized P 3p and 3s−derived states.[28,46] Feature B and C observed in the P(V) compounds have also been observed in previous studies of Na-, K-, and In-based phosphates.[27,30,46] In these studies, these features have been assigned to either multiple scattering resonances or shape resonances.[24,27,30,63] Multiple scattering resonances are a low-energy EXAFS phenomenon,[64] corresponding to the constructive interference of outgoing photoelectrons, with multiples of the nearest neighbors' backscattered photoelectron wave function.[65] The shape resonance corresponds to the resonance (i.e., electronic transition) resulting from the anisotropy of the molecular field experienced by the outgoing core electron.[66] Features B′ and C′ appearing in H$_3$P$^{(III)}$O$_3$ and Na$_2$H$_2$P$_2^{(IV)}$O$_6$ might similarly emerge from multiple scattering resonances, albeit additional analysis is needed to ascertain this assessment. The weak feature O observed around 2152.2 eV in red-P$^{(0)}$ is likely related to a superficial phosphate generated from the oxidation of elemental phosphorus.[32] In fact, this spectral feature is more prominently observed in TEY mode XANES (shown in Figure S13 in the SI). Considering that the

probing depth is smaller for TEY measurement (~20 nm for P K-edge XANES) compared to fluorescence yield (FY) measurement (~1.2 μm for P K-edge XANES), this further indicates that feature O indeed arises from the sample surface and presumably is related to the oxidation of the sample surface. The estimation of the probing depth of the TEY and FY XANES modes is outlined in Section S10 of the SI. Similar to features B and C, features D and D′ have been ascribed to shape either resonances or multiple scattering resonances in precedent studies.[24,27,30,63] This feature is sensitive to the ligand of the P-containing compounds. Feature D for the phosphorus compounds containing multiple oxygen atoms (e.g., H$_3$P$^{(III)}$O$_3$, Na$_2$H$_2$P$^{(IV)}_2$O$_6$, and all phosphates-containing materials used in this study) is also called oxygen oscillation.[18]

The P L$_{2,3}$-edge XANES data (Figure 1B) feature electron transitions from the P 2p doublet to unoccupied states formed mainly by P 3s and P 3d−derived states, with other electronic states from ligands. Due to the higher-energy resolution (~0.14 eV) and narrower natural line width (0.03 eV) of P L$_{2,3}$-edge transition compared to the P K-edge (energy resolution of ~0.58 eV and a natural line width of 0.53 eV), the P L$_{2,3}$-edge XANES exhibits more complex spectra with, as a result, a higher information content.[24,63] Details and considerations for energy resolution and natural width can be found in Section 6 in the SI. At the P L$_{2,3}$-edge, similar XANES features were observed for the phosphide compounds (GaP$^{(-III)}$ and InP$^{(-III)}$) and elemental phosphorus (red-P$^{(0)}$). The peaks a_1' and a_2' between 130 and 131 eV correspond to the transition of P 2p$_{3/2}$ and 2p$_{1/2}$ electrons, respectively, into $1e^*$-derived states.[32] The smaller feature b' at higher excitation energy may arise from superficial oxidation of the compounds,[32] and it is more prominent at the P L$_{2,3}$-edge compared to the P K-edge (i.e., feature O of red-P$^{(0)}$ in Figure 1A). Since the P K-edge transition is probed and detected by photons with higher energy compared to the L$_{2,3}$-edge transition, the attenuation length for P K-edge XANES is also larger (~1.2 μm) than that of P L$_{2,3}$-edge XANES (~0.04 μm, see details in Section S10 of the SI). Hence, the P L$_{2,3}$-edge XANES provides more surface-sensitive information compared to P K-edge XANES, and therefore a more pronounced contribution from the surface oxidation is observed with the P L$_{2,3}$-edge XANES. For the same reason, a very pronounced contribution of feature b' was observed by TEY XANES compared to XANES data collected in PFY mode, as shown in Figure S14 in the SI. Additionally, a preceding study also reported multiple features emerging around 139 and 147 eV (feature c'), referring to them as shape resonances corresponding to the P 2p to P 3d transition.[32]

Interestingly, all other oxygen-containing phosphorus compounds in Figure 1B show different P L$_{2,3}$-edge XANES spectral responses compared with the phosphides and elemental phosphorus. Na$_2$H$_2$P$^{(IV)}_2$O$_6$, H$_3$P$^{(V)}$O$_4$, and KH$_2$P$^{(V)}$O$_4$ show small peaks a_1 and a_2 at around ~139 eV, followed by a strong feature b and a broad feature c around 146 eV. The a_1 and a_2 peaks correspond to the excitation of the P 2p doublet into antibonding orbitals derived from hybridized P 3s- and O 2p σ-derived states.[24,25,29] Peak b is attributed to excitations into the t_2 orbital, related to the strong sp^3 hybridization of the P 3s- and O 2p π-derived states.[24,25,29] Feature c might be emerging from the transition of P 2p electrons into the e orbital (P 3d + O 2p σ-derived states).[24,29] Earlier studies also referred to these features as shape resonance (also called d-shape resonance in some
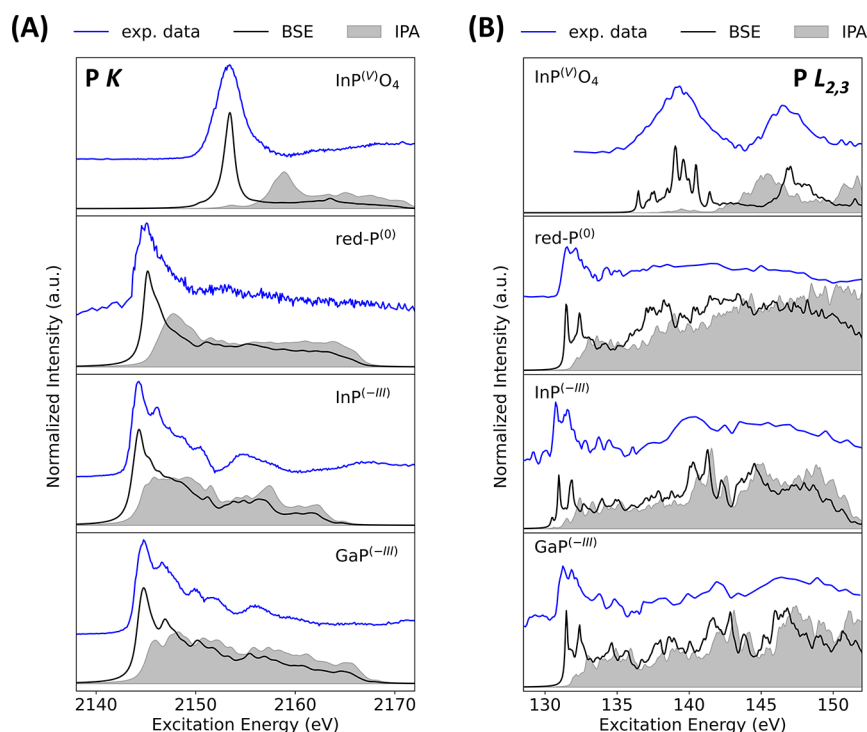
Figure 2. Experimentally derived XANES data (blue lines) of $GaP^{(-III)}$, $InP^{(-III)}$, red-$P^{(0)}$, and $InP^{(V)}O_4$ compared to *ab initio* spectra computed based on the BSE (electron−hole correlations included, black lines) and the IPA (electron−hole correlations excluded, gray areas) of the (A) P K-edge and (B) P $L_{2,3}$-edge. For better comparability between experimental and *ab initio* calculated spectra, the computational results have been broadened by 0.5 eV for P K-edge and 0.1 eV for P $L_{2,3}$-edge data to match the experimental excitation energy resolution (details for experimental energy resolution can be found at Section 9 in the SI).

works[1,3,25]). In $H_3P^{(III)}O_3$, $Na_2H_2P_2^{(IV)}O_6$, and other P(V) compounds, which all contain three or more electronegative atoms (i.e., oxygen atoms), a broad shape resonance occurs around 145−147 eV, which is in agreement with other studies.[24,25] For $Na_2HP^{(V)}O_4$, $InP^{(V)}O_4$, and $H_3P^{(III)}O_3$, the observed features between 138 and 139 eV are likely a convolution of the excitation of P 2p electrons into sp^3-hybridized σ- and π-derived states. The energy position of these features is sensitive to the local chemical environment of P-containing compounds.[24,25]

In general, even though all compounds show unique features at both the P K-edge and P $L_{2,3}$-edge, there are strong spectral similarities among compounds of the same group (phosphides or phosphates), which suggests the possibility of distinguishing between phosphorus species in different chemical environments through fingerprinting. For instance, some of the spectral features are very sensitive to the chemical environment around P atoms, such as features D', D and c', c for P K-edge and P $L_{2,3}$-edge XANES, respectively. Therefore, in the best case, these features can be directly related to specific P-ligand bond formation. At both P K-edge and P $L_{2,3}$-edge, phosphorus compounds containing several oxygen atoms (e.g., $H_3P^{(III)}O_3$, $H_3P^{(V)}O_4$) show a broad feature (e.g., feature D or c) whereas phosphide compounds with metallic ligands (e.g., $GaP^{(-III)}$, $InP^{(-III)}$) display several narrower and weaker spectral features (e.g., feature D' or c'). For the P K-edge XANES of elemental phosphorus (red-$P^{(0)}$), the latter features are not observed, since there are no ligand-scattering P-derived photoelectrons. Thus, the presence (spectral shape) or lack of the shape resonance may hint at the nature of the P ligand.

Furthermore, in both P K-edge and P $L_{2,3}$-edge XANES, there seems to be an energy shift of the spectra with the

nominal P oxidation state (see Figure 1A,B). The compounds with higher oxidation states exhibit a white line at higher excitation energy, as also observed in XANES studies with other chemical elements.[67−69] For a precise determination of the energy shift, the absorption edge was estimated (see details in Section 2.2) and the resulting shifts of the absorption-edge relative to that of red-$P^{(0)}$ are shown in Figure 1C as a function of the compounds' nominal P oxidation states. As illustrated in Figure 1C, there is a similar absorption-edge shift for nominal P oxidation states for both the P K-edge and P $L_{2,3}$-edge data.

$Na_2H_2P^{(IV)}_2O_6$ shows a slightly lower absorption-edge position compared to that of $H_3P^{(III)}O_3$, even though it possesses a higher oxidation state. Red-$P^{(0)}$ also shows a similar absorption-edge position as $GaP^{(-III)}$ even though it possesses a higher oxidation state. Likely, the geometry around the P atoms influences the electron−hole interaction, such that the P atoms in $Na_2H_2P_2O_6$ are slightly more screened compared to atoms in H_3PO_3. Similarly, the P atoms in red-P might experience similar screening to the atoms in GaP. Hence, another descriptor besides the oxidation state is needed to consider the screening effect arising from geometry around P atoms when establishing a relation to the absorption-edge position. Assuming that the biggest influence on screening arises from the P atom nearest neighbors, the nearest neighbors for these compounds are determined by using theoretical crystal structures provided in the Materials Project database.[61] Subsequently, the total electronegativity resulting from the nearest neighbors is calculated. Details can be found in Section S11 of the SI. Since electronegativity represents the ability of atoms to attract electrons,[70] it might serve as a good measure of the electronic density around P atoms and thus of screening effects. Since the nearest neighbors' electronegativity

of $Na_2H_2P^{(IV)}_2O_6$ possess a very similar electronegativity around P atoms compared to $H_3P^{(III)}O_3$, which is also the case for red-$P^{(0)}$ and $GaP^{(-III)}$, the seeming disagreement w.r.t. the absorption-edge shift disappears when representing the shift as a function of nearest neighbors' electronegativity (see Figure 1D) instead of using the nominal P oxidation state as a descriptor (see Figure 1C), supporting this approach. Of course, it is important to note that other atoms besides the nearest neighbors will also influence the screening around P atoms, although to a lesser extent. For instance, a slightly different absorption-edge position was observed for different phosphates in this study, even though all compounds have the same nearest neighbors around P atoms, i.e., four oxygen atoms. Nevertheless, even though further analysis is needed to determine the ideal descriptor representing the screening around the probed atoms, the total electronegativity of the atoms surrounding the P atoms provides good insights into the screening experienced by the P atoms. Additionally, it is important to note that the $Na_2H_2P_2O_6$ used in this study is highly hydrated ($Na_2H_2P_2O_6 \cdot 10H_2O$, see Section 2.1); hence, the interaction with H_2O might influence the coordination of the $Na_2H_2P_2O_6$, thus also affecting the absorption-edge energy positions.

To gain further insight into the electronic structure of the studied P compounds, we analyze the *ab initio* XANES calculations from both the P K-edge and the P $L_{2,3}$-edge performed on representative solid-state P-compounds, including $GaP^{(-III)}$, $InP^{(-III)}$, red-$P^{(0)}$, and $InP^{(V)}O_4$ (see Figure 2). *Ab initio* calculations were carried out for these systems, for (i) a representation of P-compounds with different oxidation states, from P(-III) to P(V), and (ii) P-compounds with similar ligands but different chemical environments (e.g., InP and $InPO_4$, both contain In^{3+} cations but are in a different environment).

First and foremost, we notice very good agreement between the BSE results and the experimentally derived spectra, especially for the P K-edge data. Note that for the experimental data given in Figure 2, a modified spectral background corresponding to the electronic transition to continuum states has been subtracted to allow a better comparison between experiments and *ab initio* calculations (as detailed in Section 2.2 and Section 2.3; the corresponding background determination can be found in Figure S15 in the SI). As visible in Figure 2A, the peak positions and oscillator strengths match very well. In particular, the calculations correctly reproduce the sharp white line characterizing the spectra of red-P and of the phosphides (InP and GaP) followed by weaker but distinct resonances. Also, the spectrum of $InPO_4$ is described well; reproducing the dominating strong peak at the onset accompanied by a very weak shoulder at lower energies (at approximately 2150 eV, Figure 2A). The comparison between the BSE spectra reported in Figure 2A (solid black lines) and their counterparts computed in the independent-particle approximation (IPA, gray areas) provides information about the role of electron−hole correlations. For instance, the maximum in the spectrum of $InPO_4$ and the weak shoulder at lower energies are present also in the IPA result, despite somewhat shifting to higher energies. However, the inclusion of the Coulomb interactions in the BSE calculations has correctly redistributed their energies and oscillator strengths, resulting in much better agreement with the experiment. The energy shift between the absorption maximum in the IPA spectrum and in the BSE calculations can be interpreted as the binding energy of the

corresponding core exciton.[58] In the case of $InPO_4$, it is in the order of ∼5 eV—similar to the values obtained at the same level of theory in organic compounds.[71] This finding suggests that coordination with oxygen substantially decreases the screening of the material, thereby enhancing the Coulomb strength between the electron−hole pairs therein. In the other spectra shown in Figure 2A, the core exciton binding energies (i.e., the absorption-edge differences in the BSE and IPA spectra) are sizeably smaller, in the order of (or even less than) 1 eV. Yet, in the spectra of red-P and of the phosphides, the electron−hole correlations (that are considered in BSE but not in IPA calculations) are essential to correctly redistribute the spectral weight at the onset and enhance the intensity of the first resonance in comparison with the higher-energy ones.

Even for the P $L_{2,3}$-edge XANES (Figure 2B), we appreciate again good agreement between the BSE and the experimental results, although the relative weights of the absorption maxima in the spectra of red-P and of the phosphides are distributed somewhat differently between the onset and the higher-energy region. The spectral features observed in the experimental data are also observed in the BSE data. The general trends discussed for the P K-edge spectra are also valid for the P $L_{2,3}$-edge data. Pronounced electron−hole interactions represented by the large difference between the BSE and IPA computed spectra are again observed for $InPO_4$, corroborating the presence of a strongly bound core exciton with a binding energy in the order of 5 eV (in agreement with the P K-edge analysis, above). For red-P, InP, and GaP, the spectral shapes of the calculated spectra are essentially unchanged by the inclusion of excitonic effects, which only systematically red-shift the oscillator strength toward lower energies by 1.0−1.5 eV for all compounds (see Figure 2B). Note that effects like thermalization are not well considered by broadening of the computational results with a constant factor (as done in Figure 2), explaining the decreasing agreement of experimental and calculated XANES spectra with increasing photon energies (e.g., photon energies above ∼137 eV for GaP, InP, or red-P in Figure 2B). This effect arises from the larger energy broadening expected at higher energies due to a shorter core-hole lifetime, which is not represented by the constant energy broadening of 0.1 eV used for the presentation of the calculated spectra to resolve the low-energy spectral features. For more details, please see the discussion in conjunction with the calculated XANES presented with a larger energy broadening (0.25 and 0.5 eV) in Figure S16 in the SI.

3.2. Aqueous P-Containing H_3PO_3, H_3PO_4, and H_3PO_3 + H_3PO_4 Mixtures.

In the final part of this study, the P K-edge XANES of H_3PO_4 and H_3PO_3, as well as their mixtures in aqueous solutions, is investigated. Figure 3 depicts the white line region of these spectra, where the most pronounced spectral change is observed (wider-range XANES data are shown in Figure S17 in the SI).

As shown in Figure 3, the P K-edge XANES from the aqueous solutions displays spectral features that are mainly analogous to the spectra of their solid counterparts (i.e., strong features at ∼2150.8 eV for H_3PO_3- and ∼2152.5 eV for H_3PO_4-containing solutions, respectively, as well as shape resonance at around 2170 eV, see Figure S17 in the SI). However, close inspection of the data reveals several spectral differences between the P K-edge XANES spectra of the aqueous acids and the spectra of their solid counterparts. A slight shift of the XANES spectra to lower excitation energies (∼0.2−0.3 eV) is observed for the aqueous solutions
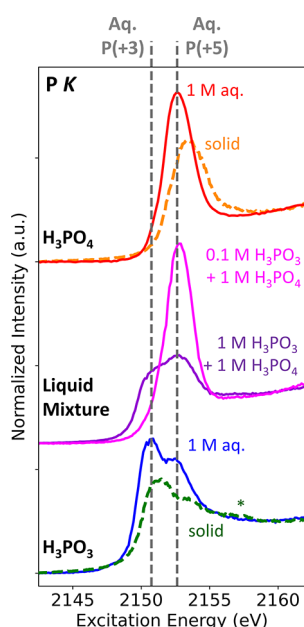
Figure 3. P K-edge XANES white line region of aqueous 1 mol dm^{-3} (1 M) H_3PO_3, 1 mol dm^{-3} (1 M) H_3PO_4, and their mixtures: 0.1 mol dm^{-3} (0.1 M) H_3PO_3 + 1 mol dm^{-3} (1 M) H_3PO_4 and 1 mol dm^{-3} (1 M) H_3PO_3 + 1 mol dm^{-3} (1 M) H_3PO_4. For comparison, the spectra of solid-state H_3PO_3 and H_3PO_4 (from Figure 1A) are also shown as dashed lines. The white line energy positions of aqueous (aq.) H_3PO_3 and H_3PO_4 are illustrated with vertical gray dashed lines. The green asterisk highlights multiple scattering features observed in solid H_3PO_3, which are not observed in aq. 1 M H_3PO_3.

compared to the solid compounds. Other XANES investigations of solid compounds and their counterparts in a liquid solution appear to show a similar phenomenon (although it is not discussed explicitly).[69,72] This behavior is likely related to the high polarity of the solvent (H_2O). In such a solvent, part of the acid salts forms an anion (e.g., the formation of $H_2PO_4^-$ anions when H_3PO_4 is diluted in H_2O).[73] The environment surrounding the phosphorus atoms is more negative in anionic form,[35] which may result in a red shift of the absorption-edge position.

Additionally, H_3PO_3 and H_3PO_4 dispersed in 1 mol dm^{-3} aqueous solutions show a higher white line intensity with respect to the edge jump (intensity ~2160 eV) compared to the solid counterparts. Due to the nature of the FY mode used for this investigation, this phenomenon can likely be explained by self-absorption,[69] less affecting the measurements of the diluted aqueous solutions compared to their solid counterparts. This is corroborated by P K-edge XANES measurements of differently concentrated aqueous H_3PO_4 solutions, exhibiting a similar trend of a white line intensity enhancement (relative to the respective edge jump) with decreasing H_3PO_4 concentration (see Figure S18 in SI).

Furthermore, aqueous H_3PO_3 exhibits different spectral features compared to its solid counterpart. Solid H_3PO_3 displayed multiple features following the white line (at ~2152.8 and 2157.5 eV [see green asterisk], labeled as B' and C' in Figure 1A). However, no related features (green asterisk in Figure 3) were observed in the spectrum of a 1 mol dm^{-3} aqueous solution of H_3PO_3. Similar observations were reported in XANES investigations of solid and solvated forms of K_2SO_4 and K_2PtCl_6.[58,59] An explanation for this observation could be the loss of degeneracy of the electronic states due to

the loss of symmetry upon deprotonation of H_3PO_3 (i.e., its solvation in an aqueous solution). Moreover, the interaction of H_3PO_3 with H_2O might significantly influence the coordination of phosphorous acid.[33,72,74]

For the aqueous mixture of 1 mol of dm^{-3} H_3PO_3 + 1 mol of dm^{-3} H_3PO_4, spectral features corresponding to the white lines of 1 mol of dm^{-3} H_3PO_3 and 1 mol of dm^{-3} H_3PO_4 are observed, respectively, suggesting the possibility of speciation and quantification through fingerprinting (in this case). However, for a mixture with a lower concentration of H_3PO_3: 0.1 mol dm^{-3} H_3PO_3 + 1 mol dm^{-3} H_3PO_4, the P K-edge XANES feature corresponding to the H_3PO_3 solution is barely visible. Only direct comparison with the spectrum of 1 mol dm^{-3} H_3PO_4 reveals some H_3PO_3-related spectral intensity below the H_3PO_4 onset (as shown in Figure S19 in the SI). It implies that even though speciation through fingerprinting is possible, for low-content solutions, such an approach might become challenging.

4. SUMMARY AND CONCLUSIONS

X-ray absorption near-edge structure (XANES) at P K-edge and P $L_{2,3}$-edge were employed to investigate the chemical and electronic structure of solid P compounds with various oxidation states and environments, as well as H_3PO_3, H_3PO_4, and their mixtures in aqueous solutions.

At both the P K-edge and P $L_{2,3}$-edge, XANES of solid compounds revealed similarities in spectra for compounds with similar oxidation states/chemical environments, enabling facile speciation through spectral fingerprinting. In particular, several of the XANES spectral features are very sensitive to the chemical environment around P atoms. For instance, compounds containing oxygen show a broad spectral feature at the post edge of both P K-edge and P $L_{2,3}$-edge XANES spectra, while phosphides with metallic ligands exhibit narrower ones.

Additionally, a similar trend of absorption-edge shifts relative to red-P$^{(0)}$ was observed in P K- and P $L_{2,3}$-edge XANES, likely caused by a different screening of core-hole interactions. Electronegativity of the nearest neighbors around P atoms was proposed as an alternative descriptor for the screening effects, showing an improved relation to absorption-edge shifts compared to the commonly used nominal P oxidation state.

Comparison of experimental and calculated absorption spectra of four P-containing compounds (red-P, GaP, InP, and InPO$_4$) revealed insights into the electronic structure. InPO$_4$ exhibited prominent electron–hole interactions with a large core exciton binding energy (~5 eV), attributed to reduced dielectric screening in an O-rich environment. Other compounds showed systematic ~1 eV red-shifts and a redistribution of oscillator strength toward the absorption onset due to excitonic effects.

In aqueous solutions, P K-edge XANES of aqueous H_3PO_3 and H_3PO_4 displayed absorption-edge shifts to lower photon energies compared to solid counterparts, likely attributed to anion formation and the effect of solvation. Furthermore, aqueous H_3PO_3 exhibited fewer spectral features compared to the solid compound, possibly due to deprotonation—resulting in a loss of electronic states' degeneracy, leading to a broadening of spectral features—and/or due to the interaction between H_3PO_3 and H_2O (e.g., solvation) influencing the coordination around the P atoms. Aqueous mixtures of H_3PO_3 and H_3PO_4 with comparable concentrations showed features corresponding to white lines of both acids, indicating the

potential for speciation using spectral fingerprinting. However, for lower-content mixtures, such an approach may pose challenges.

In conclusion, we have shown that P K-edge and P $L_{2,3}$-edge XANES are powerful techniques for characterizing P-containing compounds in solid or liquid form due to their sensitivity to the oxidation state and the chemical environment. Hence, P K-edge and P $L_{2,3}$-edge XANES measurements may serve as speciation tools for P-containing compounds in several energy conversion technologies using P-based materials, providing insights into performance-relevant mechanisms and thus paving the way for knowledge-based optimization.

■ ASSOCIATED CONTENT

Data Availability Statement

The data underlying this study are openly available in Zenodo at DOI/10.5281/zenodo.7837362, for the experimental XANES data set and DOI: 10.5281/zenodo.7839832, for the *ab initio* calculation result.

⑤ Supporting Information

The Supporting Information is available free of charge at https://pubs.acs.org/doi/10.1021/acs.jpcc.3c04704.

Specification of the phosphorus-containing compounds used in the study; absorption-edge determination for the P K-edge XANES; RIXS maps of the P $L_{2,3}$-edge of solid P-containing compounds; comparison of P $L_{2,3}$-edge XANES data collected in TFY mode and PFY mode; P L_3-edge absorption-edge determination from the P $L_{2,3}$-edge XANES; *in situ* cells for P K-edge XANES measurements of aqueous H_3PO_4 and H_3PO_3 acid—based solutions; comparison of recorded XANES spectra with spectra presented in referenced works; projected density of states (pDOS) of GaP, InP, red-P, and $InPO_4$; consideration for the absorption-edge position determination and associated uncertainties; probing depth comparison of PFY and TEY XANES spectra; determination of the total electronegativity of phosphorus' nearest neighbors; P K-edge and P $L_{2,3}$-edge XANES of GaP, InP, red-P, and $InPO_4$ along with the fitted arctan background; *ab initio* calculated P $L_{2,3}$-edge XANES spectra with different broadening; P K-edge XANES of aqueous H_3PO_4, H_3PO_3 solutions, and their mixtures; P K-edge XANES of solid H_3PO_4 and aqueous H_3PO_4 solutions of different concentrations; P K-edge XANES comparison of 1 mol dm^{-3} H_3PO_4 and 0.1 mol dm^{-3} H_3PO_3 + 1 mol dm^{-3} H_3PO_4 solutions (PDF)

■ AUTHOR INFORMATION

Corresponding Authors

Romualdus Enggar Wibowo − *Department of Interface Design, Helmholtz-Zentrum Berlin für Materialien und Energie GmbH (HZB), Berlin 12489, Germany;* ⑩ orcid.org/0000-0002-8325-0413; Email: enggar.wibowo@helmholtz-berlin.de

Caterina Cocchi − *Institute of Physics and Center for Nanoscale Dynamics (CeNaD), Carl von Ossietzky Universität Oldenburg, Oldenburg 26129, Germany;* ⑩ orcid.org/0000-0002-9243-9461; Email: caterina.cocchi@uni-oldenburg.de

Marcus Bär − *Department of Interface Design, Helmholtz-Zentrum Berlin für Materialien und Energie GmbH (HZB), Berlin 12489, Germany; Energy Materials In-Situ Laboratory Berlin (EMIL), HZB, Berlin 12489, Germany; Department of Chemistry and Pharmacy, Friedrich-Alexander-Universität Erlangen-Nürnberg (FAU), Erlangen 91058, Germany; Department of X-ray Spectroscopy at Interfaces of Thin Films, Helmholtz Institute Erlangen-Nürnberg for Renewable Energy (HI ERN), Berlin 12489, Germany;* ⑩ orcid.org/0000-0001-8581-0691; Email: marcus.baer@helmholtz-berlin.de

Authors

Raul Garcia-Diez − *Department of Interface Design, Helmholtz-Zentrum Berlin für Materialien und Energie GmbH (HZB), Berlin 12489, Germany*

Marianne van der Merwe − *Department of Interface Design, Helmholtz-Zentrum Berlin für Materialien und Energie GmbH (HZB), Berlin 12489, Germany;* ⑩ orcid.org/0000-0002-3182-1392

Daniel Duarte-Ruiz − *Institute of Physics and Center for Nanoscale Dynamics (CeNaD), Carl von Ossietzky Universität Oldenburg, Oldenburg 26129, Germany;* ⑩ orcid.org/0000-0003-2424-1397

Yang Ha − *Advanced Light Source (ALS), Lawrence Berkeley National Laboratory, Berkeley, California 94720, United States;* ⑩ orcid.org/0000-0001-5684-8420

Roberto Félix − *Department of Interface Design, Helmholtz-Zentrum Berlin für Materialien und Energie GmbH (HZB), Berlin 12489, Germany;* ⑩ orcid.org/0000-0002-3620-9899

Anna Efimenko − *Department of Interface Design, Helmholtz-Zentrum Berlin für Materialien und Energie GmbH (HZB), Berlin 12489, Germany; Energy Materials In-Situ Laboratory Berlin (EMIL), HZB, Berlin 12489, Germany*

Tomas Bystron − *Department of Inorganic Technology, University of Chemistry and Technology Prague, Prague 6 166 28, Czech Republic*

Martin Prokop − *Department of Inorganic Technology, University of Chemistry and Technology Prague, Prague 6 166 28, Czech Republic*

Regan G. Wilks − *Department of Interface Design, Helmholtz-Zentrum Berlin für Materialien und Energie GmbH (HZB), Berlin 12489, Germany; Energy Materials In-Situ Laboratory Berlin (EMIL), HZB, Berlin 12489, Germany;* ⑩ orcid.org/0000-0001-5822-8399

Karel Bouzek − *Department of Inorganic Technology, University of Chemistry and Technology Prague, Prague 6 166 28, Czech Republic*

Wanli Yang − *Advanced Light Source (ALS), Lawrence Berkeley National Laboratory, Berkeley, California 94720, United States;* ⑩ orcid.org/0000-0003-0666-8063

Complete contact information is available at:
https://pubs.acs.org/10.1021/acs.jpcc.3c04704

Author Contributions

R.E.W. carried out the hard XANES and soft XANES experiments with the support of M.v.d.M, under close supervision from R.G.-D. D.D.-R. carried out the *ab initio* XANES calculation under the supervision of C.C. Y.H. performed soft XANES characterizations on all P(V)-containing compounds with support from W.Y. R.F. provided support for hard XANES measurement at the KMC-1 beamline. A.E. optimized the CPMU17 EMIL beamline, enabling the hard XANES measurements with aqueous P-containing compounds. M.P. and T.B. carried out the synthesis

■ REFERENCES

(1) Nicholls, M. A.; Norton, P. R.; Bancroft, G. M.; Kasrai, M.; Do, T.; Frazer, B. H.; De Stasio, G. Nanometer Scale Chemomechanical Characterization of antiwear Films. *Tribol. Lett.* **2004**, *17* (2), 205−216.

(2) Nicholls, M. A.; Bancroft, G. M.; Kasrai, M.; Norton, P. R.; Frazer, B. H.; Stasio, G. D. Improvement of PEEM Images from Thick Inhomogeneous antiwear Films Using a Thin Pt Coating. *Tribol. Lett.* **2005**, *18* (4), 453−462.

(3) Pereira, G.; Lachenwitzer, A.; Munoz-Paniagua, D.; Kasrai, M.; Norton, P. R.; Abrecht, M.; Gilbert, P. U. P. A. The Role of the Cation in antiwear Films Formed from ZDDP on 52100 Steel. *Tribol. Lett.* **2006**, *23* (2), 109−119.

(4) Liu, W.; Zhi, H.; Yu, X. Recent Progress in Phosphorus Based Anode Materials for Lithium/Sodium Ion Batteries. *Energy Storage Mater.* **2019**, *16*, 290−322.

(5) Jin, H.; Zhang, T.; Chuang, C.; Lu, Y.-R.; Chan, T.-S.; Du, Z.; Ji, H.; Wan, L. Synergy of Black Phosphorus−Graphite−Polyaniline-Based Ternary Composites for Stable High Reversible Capacity Na-Ion Battery Anodes. *ACS Appl. Mater. Interfaces* **2019**, *11* (18), 16656−16661.

(6) Li, M.; Li, W.; Hu, Y.; Yakovenko, A. A.; Ren, Y.; Luo, J.; Holden, W. M.; Shakouri, M.; Xiao, Q.; Gao, X.; Zhao, F.; Liang, J.; Feng, R.; Li, R.; Seidler, G. T.; Brandys, F.; Divigalpitiya, R.; Sham, T.; Sun, X. New Insights into the High-Performance Black Phosphorus Anode for Lithium-Ion Batteries. *Adv. Mater.* **2021**, *33* (35), 2101259.

(7) Sammes, N.; Bove, R.; Stahl, K. Phosphoric Acid Fuel Cells: Fundamentals and Applications. *Curr. Opin. Solid State Mater. Sci.* **2004**, *8* (5), 372−378.

(8) Araya, S. S.; Zhou, F.; Liso, V.; Sahlin, S. L.; Vang, J. R.; Thomas, S.; Gao, X.; Jeppesen, C.; Kær, S. K. A Comprehensive Review of PBI-Based High Temperature PEM Fuel Cells. *Int. J. Hydrog. Energy* **2016**, *41* (46), 21310−21344.

(9) Qing, G.; Kikuchi, R.; Takagaki, A.; Sugawara, T.; Oyama, S. T. CsH5(PO4)2 Doped Glass Membranes for Intermediate Temperature Fuel Cells. *J. Power Sources* **2014**, *272*, 1018−1029.

(10) Schuster, M.; Kreuer, K.; Steininger, H.; Maier, J. Proton Conductivity and Diffusion Study of Molten Phosphonic Acid H3PO3. *Solid State Ionics* **2008**, *179* (15−16), 523−528.

(11) Shen, Z.-K.; Yuan, Y.-J.; Pei, L.; Yu, Z.-T.; Zou, Z. Black Phosphorus Photocatalysts for Photocatalytic H2 Generation: A Review. *Chem. Eng. J.* **2020**, *386*, No. 123997.

(12) Fung, C. M.; Er, C. C.; Tan, L. L.; Mohamed, A. R.; Chai, S. P. Red Phosphorus: An Up-and-Coming photocatalyst on the Horizon for Sustainable Energy Development and Environmental Remediation. *Chem. Rev.* **2022**, *122* (3), 3879−3965.

(13) Hu, Z.; Shen, Z.; Yu, J. C. Phosphorus Containing Materials for Photocatalytic Hydrogen Evolution. *Green Chem.* **2017**, *19* (3), 588−613.

(14) Geisz, J. F.; Steiner, M. A.; García, I.; Kurtz, S. R.; Friedman, D. J. Enhanced External Radiative Efficiency for 20.8% Efficient Single-Junction GaInP Solar Cells. *Appl. Phys. Lett.* **2013**, *103* (4), No. 041118.

(15) Batmunkh, M.; Bat-Erdene, M.; Shapter, J. G. Black Phosphorus: Synthesis and Application for Solar Cells. *Adv. Energy Mater.* **2018**, *8* (5), 1701832.

(16) Ajiboye, B.; Akinremi, O. O.; Jürgensen, A. Experimental Validation of Quantitative XANES Analysis for Phosphorus Speciation. *Soil Sci. Soc. Am. J.* **2007**, *71* (4), 1288−1291.

(17) Ajiboye, B.; Akinremi, O. O.; Hu, Y.; Flaten, D. N. Phosphorus Speciation of Sequential Extracts of Organic Amendments Using Nuclear Magnetic Resonance and X-ray Absorption Near-Edge Structure Spectroscopies. *J. Environ. Qual.* **2007**, *36* (6), 1563−1576.

(18) Kruse, J.; Leinweber, P. Phosphorus in Sequentially Extracted Fen Peat Soils: A K-Edge X-Ray Absorption near-Edge Structure (XANES) Spectroscopy Study. *J. Plant Nutr. Soil Sci.* **2008**, *171* (4), 613−620.

(19) Kruse, J.; Negassa, W.; Appathurai, N.; Zuin, L.; Leinweber, P. Phosphorus Speciation in Sequentially Extracted Agro-Industrial By-Products: Evidence from X-ray Absorption Near Edge Structure Spectroscopy. *J. Environ. Qual.* **2010**, *39* (6), 2179−2184.

(20) Luo, L.; Ma, Y.; Sanders, R. L.; Xu, C.; Li, J.; Myneni, S. C. B. Phosphorus Speciation and Transformation in Long-Term Fertilized Soil: Evidence from Chemical Fractionation and P K-Edge XANES Spectroscopy. *Nutr. Cycl. Agroecosyst.* **2017**, *107* (2), 215−226.

(21) Vogel, C.; Rivard, C.; Wilken, V.; Muskolus, A.; Adam, C. Performance of Secondary P-Fertilizers in Pot Experiments Analyzed by Phosphorus X-Ray Absorption near-Edge Structure (XANES) Spectroscopy. *Ambio* **2018**, *47* (S1), 62−72.

(22) Babos, D. V.; Castro, J. P.; Andrade, D. F.; Costa, V. C.; Pereira-Filho, E. R. Determination and Speciation of Phosphorus in Fertilizers and Mineral Supplements for Cattle by X-Ray Absorption near-Edge Structure Spectroscopy: A Simple Nondestructive Method. *Anal. Methods* **2019**, *11* (11), 1508−1515.

(23) Schmidt, S.; Sallard, S.; Borca, C.; Huthwelker, T.; Novák, P.; Villevieille, C. Phosphorus Anionic Redox Activity Revealed by *Operando* P K-Edge X-Ray Absorption Spectroscopy on Diphosphonate-Based Conversion Materials in Li-Ion Batteries. *Chem. Commun.* **2018**, *54* (39), 4939−4942.

(24) Yin, Z.; Kasrai, M.; Bancroft, G. M.; Tan, K. H.; Feng, X. X-Ray-Absorption Spectroscopic Studies of Sodium Polyphosphate Glasses. *Phys. Rev. B* **1995**, *51* (2), 742−750.

(25) Kruse, J.; Leinweber, P.; Eckhardt, K.-U.; Godlinski, F.; Hu, Y.; Zuin, L. Phosphorus L $_{2,3}$ -Edge XANES: Overview of Reference Compounds. *J. Synchrotron Rad* **2009**, *16* (2), 247−259.

(26) Nicholls, M. A.; Bancroft, G. M.; Norton, P. R.; Kasrai, M.; De Stasio, G.; Frazer, B. H.; Wiese, L. M. Chemomechanical Properties of antiwear Films Using X-Ray Absorption Microscopy and Nanoindentation Techniques. *Tribol. Lett.* **2004**, *17* (2), 245−259.

(27) Demirkiran, H.; Hu, Y.; Zuin, L.; Appathurai, N.; Aswath, P. B. XANES Analysis of Calcium and Sodium Phosphates and Silicates and Hydroxyapatite−Bioglass®45S5 Co-Sintered Bioceramics. *Mater. Sci. Eng: C* **2011**, *31* (2), 134−143.

(28) Oizumi, H.; Iizuka, J.; Oyanagi, H.; Fujikawa, T.; Ohta, T.; Usami, S. K-Edge XANES of GaP, InP and GaSb. *Jpn. J. Appl. Phys.* **1985**, *24* (Part1, No. 11), 1475−1478.

(29) Kucheyev, S. O.; Bostedt, C.; van Buuren, T.; Willey, T. M.; Land, T. A.; Terminello, L. J.; Felter, T. E.; Hamza, A. V.; Demos, S. G.; Nelson, A. J. Electronic Structure of K D 2 x H 2 (1 − x) P O 4 Studied by Soft x-Ray Absorption and Emission Spectroscopies. *Phys. Rev. B* **2004**, *70* (24), No. 245106.

(30) Li, X.; Liu, B.; Yan, C.; Liu, C.; Ju, X. Investigating the Surface Electronic Structures of Retired Components and Irradiated KDP Crystals with Different Fluences by XANES Spectroscopy. *Opt. Mater. Express* **2018**, *8* (4), 816.

(31) Domashevskaya, E. P.; Kashkarov, V. M.; Seredin, P. V.; Terekhov, V. A.; Turishchev, S. Yu.; Arsentyev, I. N.; Ulin, V. P. Investigation of Porous InP by X-Ray Diffraction, IR Spectroscopy, USXES, XANES Spectroscopy, and Photoluminescence. *Bull. Russ. Acad. Sci. Phys.* **2008**, *72* (4), 439−442.

(32) Jrgensen, A. The P1s and P2p XAFS Spectra of Elemental Phosphorus, Theory and Experiment. *Phys. Scr.* **2005**, *2005* (T115), 546−551.

(33) Rouff, A. A.; Rabe, S.; Nachtegaal, M.; Vogel, F. X-Ray Absorption Fine Structure Study of the Effect of Protonation on Disorder and Multiple Scattering in Phosphate Solutions and Solids. *J. Phys. Chem. A* **2009**, *113* (25), 6895−6903.

(34) Persson, I.; Trublet, M.; Klysubun, W. Structure Determination of Phosphoric Acid and Phosphate Ions in Aqueous Solution Using EXAFS Spectroscopy and Large Angle X-Ray Scattering. *J. Phys. Chem. A* **2018**, *122* (37), 7413−7420.

(35) Persson, I.; Klysubun, W.; Lundberg, D. A K-Edge P XANES Study of Phosphorus Compounds in Solution. *J. Mol. Struct.* **2019**, *1179*, 608−611.

(36) Sugishima, N.; Hinatsu, J. T.; Foulkes, F. R. Phosphorous acid Impurities in Phosphoric Acid Fuel Cell Electrolytes: II. Effects on the Oxygen Reduction Reaction at Platinum Electrodes. *J. Electrochem. Soc.* **1994**, *141* (12), 3332.

(37) Prokop, M.; Kodym, R.; Bystron, T.; Paidar, M.; Bouzek, K. Degradation Kinetics of Pt during High-Temperature PEM Fuel Cell Operation Part I: Kinetics of Pt Surface Oxidation and Dissolution in Concentrated H3PO4 Electrolyte at Elevated Temperatures. *Electrochim. Acta* **2019**, *313*, 352−366.

(38) Prokop, M.; Bystron, T.; Bouzek, K. Electrochemistry of Phosphorous and Hypophosphorous Acid on a Pt Electrode. *Electrochim. Acta* **2015**, *160*, 214−218.

(39) Prokop, M.; Bystron, T.; Paidar, M.; Bouzek, K. H3PO3 Electrochemical Behaviour on a Bulk Pt Electrode: Adsorption and Oxidation Kinetics. *Electrochim. Acta* **2016**, *212*, 465−472.

(40) Gomes, B. F.; Prokop, M.; Bystron, T.; Loukrakpam, R.; Melke, J.; Lobo, C. M. S.; Fink, M.; Zhu, M.; Voloshina, E.; Kutter, M.; Hoffmann, H.; Yusenko, K. V.; Buzanich, A. G.; Röder, B.; Bouzek, K.; Paulus, B.; Roth, C. Following Adsorbed Intermediates on a Platinum Gas Diffusion Electrode in H $_3$ PO $_3$ -Containing Electrolytes Using In Situ X-Ray Absorption Spectroscopy. *ACS Catal.* **2022**, *12* (18), 11472−11484.

(41) Romanyuk, O.; Supplie, O.; Paszuk, A.; Stoeckmann, J. P.; Wilks, R. G.; Bombsch, J.; Hartmann, C.; Garcia-Diez, R.; Ueda, S.; Bartoš, I.; Gordeev, I.; Houdkova, J.; Kleinschmidt, P.; Bär, M.; Jiříček, P.; Hannappel, T.; et al. Hard X-ray Photoelectron Spectroscopy Study of Core Level Shifts at Buried GaP/Si(001) Interfaces. *Surf. Interface Anal.* **2020**, *52* (12), 933−938.

(42) Favaro, M.; Clark, P. C. J.; Sear, M. J.; Johansson, M.; Maehl, S.; van de Krol, R.; Starr, D. E. Spectroscopic Analysis with Tender X-Rays: SpAnTeX, a New AP-HAXPES End-Station at BESSY II. *Surf. Sci.* **2021**, *713*, No. 121903.

(43) Gorgoi, M.; Svensson, S.; Schäfers, F.; Öhrwall, G.; Mertin, M.; Bressler, P.; Karis, O.; Siegbahn, H.; Sandell, A.; Rensmo, H.; Doherty, W.; Jung, C.; Braun, W.; Eberhardt, W.; et al. The High Kinetic Energy Photoelectron Spectroscopy Facility at BESSY Progress and First Results. *Nucl. Instrum. Methods Phys. Res. A: Accel. Spectrom. Detect. Assoc. Equip.* **2009**, *601* (1−2), 48−53.

(44) Schaefers, F.; Mertin, M.; Gorgoi, M. KMC-1: A High Resolution and High Flux Soft x-Ray Beamline at BESSY. *Rev. Sci. Instrum.* **2007**, *78* (12), 123102.

(45) Moulder, J. F., Stickle, W. F., Sobol, P. E., Bomben, K. D. *Handbook of X-Ray Photoelectron Spectroscopy: A Reference Book of Standard Spectra for Identification and Interpretation of XPS Data*; Physical Electronics, Incorporation, Eds. Physical Electronics: Eden Prairie, Minn., 1995.

(46) Franke, R.; Hormes, J. The P K-near Edge Absorption Spectra of Phosphates. *Phys. B: Condens. Matter* **1995**, *216* (1−2), 85−95.

(47) Newville, M.; Otten, R.; Nelson, A.; Ingargiola, A.; Stensitzki, T.; Allan, D.; Fox, A.; Carter, F.; Michał; Osborn, R.et al.*Lmfit/Lmfit-Py: 1.0.3*;Zenodo, 2021.

(48) Wong, J.; Lytle, F. W.; Messmer, R. P.; Maylotte, D. H. K -Edge Absorption Spectra of Selected Vanadium Compounds. *Phys. Rev. B* **1984**, *30* (10), 5596−5610.

(49) Choy, J. H.; Kim, D. K.; Demazeau, G.; Jung, D. Y. LIII-Edge XANES Study on Unusually High Valent Iridium in a Perovskite Lattice. *J. Phys. Chem.* **1994**, *98* (25), 6258−6262.

(50) Qiao, R.; Li, Q.; Zhuo, Z.; Sallis, S.; Fuchs, O.; Blum, M.; Weinhardt, L.; Heske, C.; Pepper, J.; Jones, M.; Brown, A.; Spucces, A.; Chow, K.; Smith, B.; Glans, P. A.; Chen, Y.; Yan, S.; Pan, F.; Piper, L. F. J.; Denlinger, J.; Guo, J.; Hussain, Z.; Chuang, Y. D.; Yang, W. High-Efficiency *in Situ* Resonant Inelastic x-Ray Scattering (iRIXS) Endstation at the Advanced Light Source. *Rev. Sci. Instrum.* **2017**, *88* (3), No. 033106.

(51) Jia, J. J.; Callcott, T. A.; Yurkas, J.; Ellis, A. W.; Himpsel, F. J.; Samant, M. G.; Stöhr, J.; Ederer, D. L.; Carlisle, J. A.; Hudson, E. A.; Terminello, L. J.; Shuh, D. K.; Perera, R. C. C. First Experimental Results from IBM/TENN/TULANE/LLNL/LBL Undulator Beamline at the Advanced Light Source. *Rev. Sci. Instrum.* **1995**, *66* (2), 1394−1397.

(52) van Aken, P. A.; Liebscher, B. Quantification of Ferrous/Ferric Ratios in Minerals: New Evaluation Schemes of Fe L 23 Electron Energy-Loss near-Edge Spectra. *Phys. Chem. Min.* **2002**, *29* (3), 188−200.

(53) Stoyanov, E.; Langenhorst, F.; Steinle-Neumann, G. The Effect of Valence State and Site Geometry on Ti L3,2 and O K Electron Energy-Loss Spectra of TixOy Phases. *Am. Mineral.* **2007**, *92* (4), 577−586.

(54) Piacentini, M.; Khumalo, F. S.; Olson, C. G.; Anderegg, J. W.; Lynch, D. W. Optical Transitions, XPS, Electronic States in NiPS3. *Chem. Phys.* **1982**, *65* (3), 289−304.

(55) Rosenberg, R. A.; LaRoe, P. R.; Rehn, V.; Loubriel, G. M.; Thornton, G. Soft-x-Ray Photoelectron-Yield Spectrum of InP(110) from 65 to 195 EV. *Phys. Rev. B* **1983**, *28* (10), 6083−6085.

(56) Dudzik, E.; Müller, C.; McGovern, I. T.; Lloyd, D. R.; Patchett, A.; Zahn, D. R. T.; Johal, T.; McGrath, R. H2S Adsorption on the (110) Surfaces of III−V Semiconductors. *Surf. Sci.* **1995**, *344* (1−2), 1−10.

(57) Kwok, R. W. M.; Huang, L. J.; Lau, W. M.; Kasrai, M.; Feng, X.; Tan, K.; Ingrey, S.; Landheer, D. X-Ray Absorption near Edge Structures of Sulfur on Gas-Phase Polysulfide Treated InP Surfaces and at SiN x /InP Interfaces. *J. Vac. Sci. Technol., A* **1994**, *12* (5), 2701−2704.

(58) Vorwerk, C.; Cocchi, C.; Draxl, C. Addressing Electron-Hole Correlation in Core Excitations of Solids: An All-Electron Many-Body Approach from First Principles. *Phys. Rev. B* **2017**, *95* (15), No. 155121.

(59) Vorwerk, C.; Aurich, B.; Cocchi, C.; Draxl, C. Bethe−Salpeter Equation for Absorption and Scattering Spectroscopy: Implementation in the Exciting Code. *Electron. Struct.* **2019**, *1* (3), No. 037001.

(60) Gulans, A.; Kontur, S.; Meisenbichler, C.; Nabok, D.; Pavone, P.; Rigamonti, S.; Sagmeister, S.; Werner, U.; Draxl, C. Exciting: A Full-Potential All-Electron Package Implementing Density-Functional Theory and Many-Body Perturbation Theory. *J. Phys.: Condens. Matter* **2014**, *26* (36), No. 363202.

(61) Jain, A.; Ong, S. P.; Hautier, G.; Chen, W.; Richards, W. D.; Dacek, S.; Cholia, S.; Gunter, D.; Skinner, D.; Ceder, G.; Persson, K. A. Commentary: The Materials Project: A Materials Genome Approach to Accelerating Materials Innovation. *APL Materials* **2013**, *1* (1), No. 011002.

(62) Tao, J.; Perdew, J. P.; Tang, H.; Shahi, C. Origin of the Size-Dependence of the Equilibrium van Der Waals Binding between Nanostructures. *J. Chem. Phys.* **2018**, *148* (7), No. 074110.

(63) Xiong, W.; Peng, J.; Hu, Y. Use of X-Ray Absorption near Edge Structure (XANES) to Identify Physisorption and Chemisorption of Phosphate onto Ferrihydrite-Modified Diatomite. *J. Colloid Interface Sci.* **2012**, *368* (1), 528−532.

(64) Blanchard, P. E. R.; Grosvenor, A. P.; Cavell, R. G.; Mar, A. X-Ray Photoelectron and Absorption Spectroscopy of Metal-Rich Phosphides M2P and M3P (M = Cr−Ni). *Chem. Mater.* **2008**, *20* (22), 7081−7088.

(65) Franke, R. X-Ray Absorption and Photoelectron Spectroscopy Investigation of Binary Nickelphosphides. *Spectrochim. Acta Part A* **1997**, *53* (7), 933−941.

(66) Bodeur, S.; Nenner, I.; Millie, P. Resonances in Photoabsorption Spectra of SiF_4, $Si(CH_3)_4$, and $SiCl_4$ near the Silicon K Edge. *Phys. Rev. A* **1986**, *34* (4), 2986−2997.

(67) Paris, E.; Giuli, G.; Carroll, M. R.; Davoli, I. THE VALENCE AND SPECIATION OF SULFUR IN GLASSES BY X-RAY ABSORPTION SPECTROSCOPY. *Can. Mineral.* **2001**, *39* (2), 331−339.

(68) Siebert, A.; Dou, X.; Garcia-Diez, R.; Buchholz, D.; Félix, R.; Handick, E.; Greco, G.; Hasa, I.; Wilks, R. G.; Passerini, S. Monitoring the Sodiation Mechanism of Anatase TiO_2 Nanoparticle-Based Electrodes for Sodium-Ion Batteries by *Operando* XANES Measurements. *ACS Appl. Energy Mater.* **2021**, *4* (1), 164−175.

(69) Almkvist, G.; Boye, K.; Persson, I. K -Edge XANES Analysis of Sulfur Compounds: An Investigation of the Relative Intensities Using Internal Calibration. *J. Synchrotron. Rad.* **2010**, *17* (5), 683−688.

(70) *Principles and Applications of Quantum Chemistry*; Elsevier, 2016. DOI: 10.1016/C2014-0-05143-X.

(71) Cocchi, C.; Draxl, C. Bound Excitons and Many-Body Effects in x-Ray Absorption Spectra of Azobenzene-Functionalized Self-Assembled Monolayers. *Phys. Rev. B* **2015**, *92* (20), No. 205105.

(72) Sham, T. K. X-ray Absorption near Edge Structure (XANES) of $PtCl_4^{2-}$ in Solid and Solution Environments. *J. Chem. Phys.* **1986**, *84* (12), 7054−7055.

(73) Elmore, K. L.; Hatfield, J. D.; Dunn, R. L.; Jones, A. D. Dissociation of Phosphoric Acid Solutions at 25° [1]. *J. Phys. Chem.* **1965**, *69* (10), 3520−3525.

(74) Pin, S.; Huthwelker, T.; Brown, M. A.; Vogel, F. Combined Sulfur K-Edge XANES−EXAFS Study of the Effect of Protonation on the Sulfate Tetrahedron in Solids and Solutions. *J. Phys. Chem. A* **2013**, *117* (35), 8368−8376.

(75) Hunter, J. D. Matplotlib: A 2D Graphics Environment. *Comput. Sci. Eng.* **2007**, *9* (3), 90−95.